Journal of Engineering Science and Technology Review 17 (1) (2024) 45 - 53

Research Article

JOURNAL OF
Engineering Science and Technology Review

www.jestr.org

Monitoring and Prediction of Surface Subsidence in Mining Areas by Integrating SBAS-InSAR and ELM

Ning Gao* and Qianhong Pu

School of Geomatics and Urban Spatial Informatics, Henan University of Urban Construction, Pingdingshan 467036, China

Received 9 November 2023; Accepted 25 January 2024

Abstract

With the rapid economic development in China, coal resources are being exploited greatly, which easily causes geological disasters due to surface subsidence. Fast and accurate surface subsidence monitoring and forecasting in mining regions are important references to analyze surface variation laws and disaster warning. However, differential interferometric synthetic aperture radar (D-InSAR) in mine surface monitoring is highly sensitive to spatiotemporal baseline and atmospheric delay. In addition, traditional machine learning algorithms have complicated network structures and difficulties determining parameters. Small baseline subsets InSAR (SBAS-InSAR) and extreme learning machine (ELM) dynamic prediction were combined for corresponding experimental studies to address these problems. On the basis of SBAS-InSAR, surface subsidence monitoring data in mining areas in Pingdingshan City, China, were collected, and a comparative analysis of D-InSAR monitoring data was performed, which verified the validity of SBAS-InSAR monitoring. On the basis of SBAS-InSAR data, a prediction model was built by ELM. The model results were compared with the prediction results of back propagation (BP) neural network and support vector machine (SVM) through root mean square error (RMSE) and mean relative error (MRE). Results demonstrate that the surface subsidence prediction of SBAS-InSAR in the monitoring mining area can reach millimeter accuracy. The MRE values of ELM, BP, and SVM prediction are maintained within 2%, 5%, and 8%, and the RMSE values are less than 3 mm, 7 mm, and 10 mm, respectively, thereby indicating that ELM prediction has high accuracy and reliability. This study provides an important evidence for safe production and scientific disaster prevention and reduction in mining areas.

Keywords: Mine surface subsidence, SBAS-InSAR, ELM, Monitoring, Prediction

1. Introduction

With the rapid economic development and increasing energy demand in China, the demand for coals is increasing gradually, thus expanding the mining scale continuously [1]. Following the extensive use of coal resources, the natural stress state of surrounding rocks in the working section and the original balanced stress state in overlying strata will be destroyed, thus causing redistribution of stresses. This condition further causes deformation, movement, collapse, and rupture of overlying strata in the working section, which will be finally transmitted to the surface and thereby cause surface subsidence. Surface subsidence has many hazards, such as destroying surface buildings, large-scale farmlands, and forest vegetation, and threatening the lives and properties of residents in the mining area. Hence, effective monitoring and prediction are important to prevent disasters and reduce disasters.

At present, major technologies for surface subsidence monitoring include geodetic surveying, global navigation satellite system (GNSS), measuring robots, interferometric synthetic aperture radar (InSAR), and three-dimensional laser scanning. Geodetic surveying carries out regular monitoring of discrete deformation points in mining areas by using a level, total station, and other devices. This method can acquire high-accuracy deformation information but has a high workload and a small monitoring scope. Moreover, it is easily influenced by terrain and weather and has difficulty meeting the coverage needs of high-frequency and large-area subsidence monitoring [2]. Measuring robots and three-dimensional laser scanning technology can acquire millimeter-level monitoring accuracy but require abundant economic costs.

InSAR is a spatial measurement method that has developed quickly in recent years and is widely applied to various fields, such as urban surface subsidence monitoring [3], earthquake monitoring [4], landslide monitoring in mountainous regions [5], subsidence monitoring in mining areas [6], and glacier monitoring [7]. It has the advantages of large monitoring scope and low cost. At present, surface subsidence prediction methods can generally be classified into two types: model driven and data driven [8]. Model-driven methods make recursive prediction based on surface subsidence deformation data and full geotechnical information and are represented by probability integral method, finite element method, Kalman filtering, and gray system theory. These methods are mainly based on many theoretical hypotheses in practical applications. However, they have difficulty acquiring geotechnical information, showing poor model accuracy. Data-driven methods use model-applicable data and create new calculation models creatively and adaptively according to different types of data. They are highly concerned with the development of machine learning and have gradually become the mainstream.

On this basis, many studies on surface subsidence monitoring and prediction have been reported. However, few studies have been conducted on applications based on

*E-mail address: gaoninghaoyun@163.com
ISSN: 1791-2377
doi:10.25103/jestr.171.07

InSAR time series data coupling machine learning. Hence, searching for methods and technologies that are more appropriate for InSAR deformation data analysis and perform surface subsidence prediction accurately and effectively is a problem that must be solved. In this study, surface subsidence monitoring and prediction were investigated by integrating InSAR technology and machine learning to provide references for dynamic monitoring and accurate prediction in mining areas.

2. State of the art

Extensive studies have been conducted by scholars on surface deformation monitoring and prediction. With respect to monitoring, several improved InSAR technologies have been proposed, such as differential interferometric synthetic aperture radar (D-InSAR), persistent scatterer InSAR (PS-InSAR), and small baseline subsets InSAR (SBAS-InSAR) [9]. Rafiei Fatemeh et al. [10] analyzed surface subsidence of an agricultural plain in Samalghan, Iran, by using D-InSAR data and found that groundwater overdraft was the cause of local subsidence. PérezFalls Zenia et al. [11] studied surface subsidence of the coastal plain in Tabasco based on D-InSAR technology and disclosed the possible relationship between oil–gas exploitation and surface deformation. Ou et al. [12] monitored surface deformation through D-InSAR and found that D-InSAR could acquire high-accuracy deformation information and without high gradient deformation. To realize long-term deformation monitoring, Boukhemacha M A et al. [13] applied PS-InSAR for surface deformation monitoring in Romania and compared it with traditional monitoring technologies. They proved that PS-InSAR could evaluate surface deformation in cities and potential non-urban environment. Tripathi A et al. [14] analyzed the correlation between displacement acquired by PS-InSAR and average groundwater fluctuation, which was applied to analyze surface subsidence charting of cities in India, achieving a satisfactory effect. Govil H et al. [15] studied monitoring and ground survey by using PS-InSAR and identified major causes of surface deformation. PS-InSAR solves the spatiotemporal discorrelation and atmospheric delay of D-InSAR well, but it is not completely mature theoretically. In-depth studies with experimental analysis are needed. Li et al. [16] analyzed surface inclination and curvature in mining areas by using SBAS-InSAR and provided a feasible method. Umarhadi D et al. [17] monitored and analyzed surface changes in Bergkalis Island, Indonesia, by using SBAS-InSAR, which further verified the validity of SBAS-InSAR. During SBAS-InSAR-based monitoring, the interference pair increases due to the free interference combination of radar images, and sufficient redundant observations were obtained, resulting in looser requirements on radar image quantity than those of PS-InSAR. Moreover, this approach overcomes spatiotemporal discorrelation indirectly because of the increased temporal sampling rate.

With regard to surface subsidence prediction, Xiao et al. [18] predicted surface subsidence in cities in northwest Yunnan, China, by using backpropagation (BP) neural network supported by SBAS-InSAR. Although the prediction accuracy met engineering needs, the BP network required a long time for iterative calculation because it has many structural parameters and was easily caught in the local minimum. Zhou et al. [19] optimized BP by using particle swarm optimization (PSO) to increase the convergence rate. Although PSO can improve BP prediction performances to some extent, it also involves more network parameters, making it difficult to optimize parameters. Chen et al. [20] combined D-InSAR technology and support vector machine (SVM) to predict highway deformation above the gob. Results showed that SVM could acquire relatively reliable prediction results, but they found that SVM was sensitive to penalty factor and kernel function parameters. Kong et al. [21] constructed the surface subsidence prediction model of mining areas by using four machine learning algorithms: extreme learning machine (ELM), BP neural network, SVM, and random forest. A comparative analysis based on 100 field engineering samples was carried out, which showed that ELM had the minimum fitness function.

Existing studies mainly acquired monitoring data through D-InSAR and PS-InSAR and then predicted surface subsidence by using traditional machine learning algorithms such as BP and SVM. However, few studies have been conducted on the integration of monitoring based on SBAS-InSAR and prediction based on new machine learning algorithms. Therefore, this study acquired surface monitoring data in mining areas by using SBAS-InSAR and predicted surface subsidence by introducing ELM to provide data support and decision-making support to safe exploitation and disaster control in mining areas.

The remainder of this study is organized as follows. Section 3 describes the principles of SBAS-InSAR and the ELM algorithm. A detailed test scheme of surface subsidence monitoring and prediction in mining areas based on SBAS-InSAR and ELM is designed thoroughly. Section 4 studied the effectiveness of the combination of SBAS-InSAR and ELM in surface subsidence monitoring and prediction in mining areas. Section 5 summarizes the relevant conclusions.

3. Methodology

3.1 SBAS-InSAR technical principle

SBAS-InSAR is improved based on the traditional D-InSAR technology. Its working principle is introduced as follows. According to interference combination conditions, N+1 SAR images are divided into several subsets according to multiple main images. M interference image pairs are gained by choosing appropriate spatial-temporal baseline thresholds. Differential interferograms are produced after the topographic phases and flat earth effect are removed, followed by filtering and phase unwrapping. Finally, high-accuracy time series deformation quantity is calculated by singular value decomposition or the least squares method [22].

Suppose $N+1$ SAR images combine freely and randomly in the period of t_i ($i = 1,2,\cdots,N$) and M interference pairs are produced.

$$(N+1)/2 \le M \le N(N+1)/2 \tag{1}$$

Differential interference is performed on images acquired at t_a and t_b, thus obtaining interferograms. The unwrapping phases at the azimuth and diagonal coordinates(x, r) are

$$\begin{aligned}\delta\phi(t_{ab},x,r) &= \phi(t_b,x,r)-\phi(t_a,x,r)\\ &\approx \phi_j^{def}(t_{ab},x,r)+\phi_j^{topo}(t_{ab},x,r)\\ &+\phi_j^{atm}(t_{ab},x,r)+\phi_j^{noise}(t_{ab},x,r)\end{aligned} \quad (2)$$

where $\phi(t_a,x,r)$ and $\phi(t_b,x,r)$ are the phase position of SAR images at t_a and t_b, $\phi_j^{def}(t_{ab},x,r)$ represents the phase position of line of sight (LOS) from t_a and t_b, $\phi_j^{topo}(t_{ab},x,r)$ refers to the topographic phase error, $\phi_j^{atm}(t_{ab},x,r)$ is the atmospheric error, and $\phi_j^{noise}(t_{ab},x,r)$ is the noise error.

After the topographic phase, atmospheric, and noise errors are eliminated, the interferometric phase is

$$\begin{aligned}\delta\phi_j(t_{ab},x,r) &= \phi_j^{def}(t_{ab},x,r)\\ &= 4\pi/\lambda[d(t_b,x,r)-d(t_a,x,r)]\end{aligned} \quad (3)$$

λ represents the wavelength of the radar signal, $d(t_a,x,r)$ and $d(t_b,x,r)$ are the cumulative deformation quantity of LOS at t_a and t_b in relative to the reference moment t_0, respectively.

A total of M interference pairs are acquired interferometric phases, and the matrix expression is

$$\delta\phi(x,r) = A\phi(x,r) \quad (4)$$

A denotes the $M\times N$ matrix. The determinants and permanents of the matrix represent the interferograms and images at a moment, respectively. The main image and auxiliary images are expressed by 1 and -1, respectively. The rest is expressed by 0.

When $M \geq N$, $R(A) \geq N$. The estimation value of ϕ can be calculated.

$$\hat{\phi} = (A^T A)A^{-1}\delta\phi(x,r) \quad (5)$$

3.2 Principle of the ELM algorithm

ELM is a new feed forward neural network [23]. For N observation data (x_i,t_i), where $x_i=[x_{i1},x_{i2},\cdots,x_{im}]^T$ represents the network input, $t_i=[t_{i1},t_{i2},\cdots,t_{im}]^T$ represents the network expected output, and L ($L \leq N$) is number of hidden layer nodes, and $g(x)$ is the network excitation function. The mathematical model of ELM is

$$y_i=\sum_{i=1}^{L}\beta_i g_i(x_j)=\sum_{i=1}^{L}\beta_i g(a_i x_j+b_i) \quad j=1,2,\cdots N \quad (6)$$

where y_i is the output of ELM, β_i is the weight that connects the hidden layer node and the output layer node, a_i is the weight that connects the input layer node and the hidden layer node ,and b_i is the bias of node of the hidden layer. The excitation function can be one of three types: sigmoid, hardlim, and Sin.

ELM can approximate to any N samples at zero error. Then,

$$\sum_{i=1}^{L}\|y_i-t_i\|=0 \quad (7)$$

According to Eq. (7), Eq. (6) can be expressed as:

$$y_i=\sum_{i=1}^{L}\beta_i g_i(x_j)=\sum_{i=1}^{L}\beta_i g(a_i x_j+b_i)=t_i \quad (8)$$

The matrix can be expressed as:

$$H\beta = T \quad (9)$$

where H and T are the output matrix of the hidden layer and the output of the network, respectively.

$$\begin{aligned}&Minimize:\|\mathrm{H}\cdot\beta-y\| \quad and \quad \|\beta\|\\ &s.t.\sum_{i=1}^{L}\beta_i g(a_i x_j+b_i)=y_j \quad j=1,2,\cdots N\end{aligned} \quad (10)$$

When $g(x)$ is infinitely differentiable, if network parameters a_i and b_i are given randomly, then H is constant. Hence, the training process of ELM can be viewed as calculating the least squares solution of $H\beta=T$ about $\hat{\beta}$.

$$\hat{\beta}=H^{+}T \quad (11)$$

H^{+} is the Moore-Penrose generalized inversion of H. On the basis of the above deduction, only L and $g(x)$ have to be determined during ELM training. $\hat{\beta}=(H^TH)^{-1}H^TT$ can be calculated. $\hat{\beta}$ is solved based on the least squares method, which is why it has uniqueness and global optimization, as well as strong generalization ability in theory.

3.3 Subsidence monitoring test in mining areas

The testing mining area is in the middle of Pingdingshan City, Henan Province, China. The geologic structure is mainly a fold structure. The terrain is high in the west and low in the east. Wells have been built in the mining area since 1955 for exploitation of coal resources. Pingdingshan has many production wells, such as Mine 1, Mine 2, Mine 3, and Xiangshan Mine. With the intensive exploitation of coal resources has led to continuous expansion of the gob and intensifying surface subsidence, thus bringing significant potential safety hazards. The digital elevation model (DEM) of the mining area is depicted in Fig. 1.

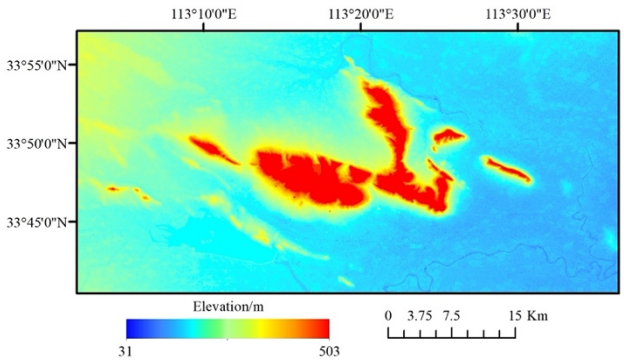

Fig. 1. DEM of the study area

Sentinel-1A image data of 21 scenes from March 5, 2022, to March 12, 2023, were collected. The selection period of image data was from 12 days to 24 days, and the corresponding 30 m DEM data and precise orbit

ephemerides data were collected. The Sentinel-1A data parameters are indicated in Table 1.

On the basis of the above data, the method based on the integration of SBAS-InSAR and ELM was established.

Its working procedures are shown in Fig. 2.

Table 1. Sentinel-1 A data parameters

Wavelength /cm	5.63
Imaging mode	Interferometric wide swath
Polarization mode	Vertical polarization
Orbital direction	Rail lift
Data type	Single-look complex
Resolution /m	5 × 20

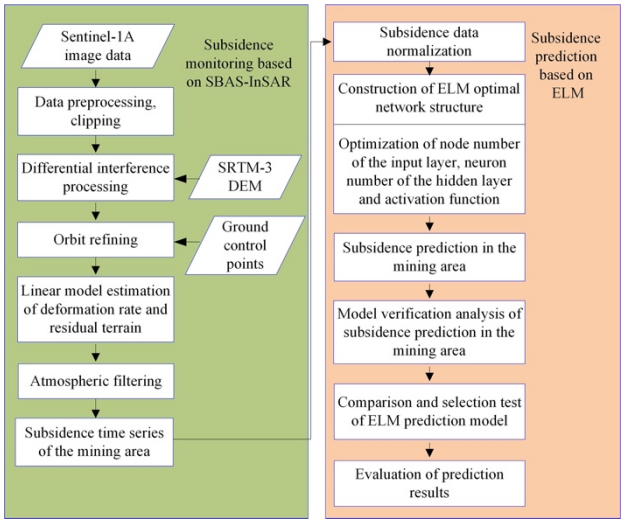

Fig. 2. The procedures based on the integration of SBAS-InSAR and ELM

4. Result Analysis and Discussion

4.1 Monitoring of mining settlement

The SAR image data of 21 scenes were clipped and the maximum time baseline was set to 180 days. The threshold of the spatial maximum critical baseline was set as 45%. The 20220901 image was chosen as the super master image, and a total of 52 interference pairs were produced.

The visual ratio of azimuth and distance direction was set to 5:1 to increase radiation resolution. The Sentinel-1A precision track file and SRTM-3 DEM data were applied to level and eliminate topographic phases. Next, image filtering and phase unwrapping were performed by using the Goldstein method and minimum cost flow, thus generating a differential interferogram. Fig. 3 shows a relatively ideal partial filtering interferogram. The phase information is clearer and noises are decreased after filtering.

A total of 31 ground control points were chosen for orbit refining and re-leveling, thus removing the residual slope phases and constant phases. Deformation rate and residual terrain were estimated by the linear model, followed by atmospheric filtering. Finally, the deformation inversion results were transformed by geocoding from the SAR coordinate system to the geographic coordinate system, thus obtaining the LOS deformation rate and cumulative subsidence volume of the study area from March 5, 2022 to March 12, 2023. The results are shown in Figs. 4 and 5.

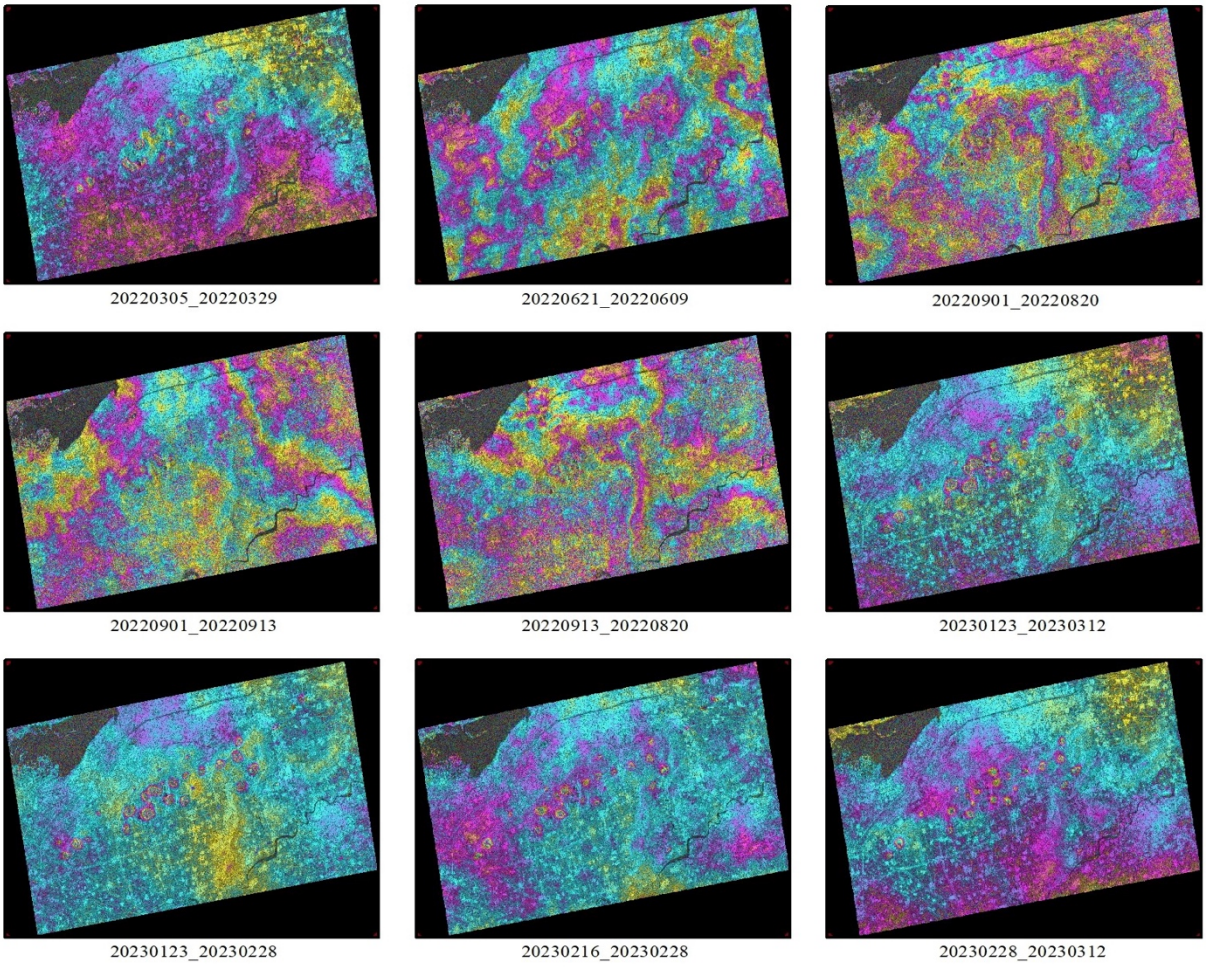

Fig. 3. Partial filtering interferogram of the study area

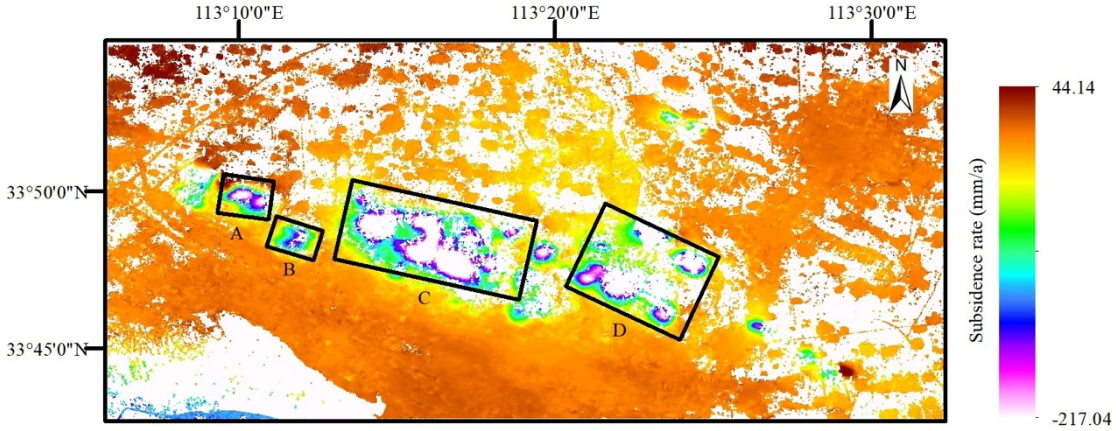

Fig. 4. Subsidence rate of SBAS-InSAR

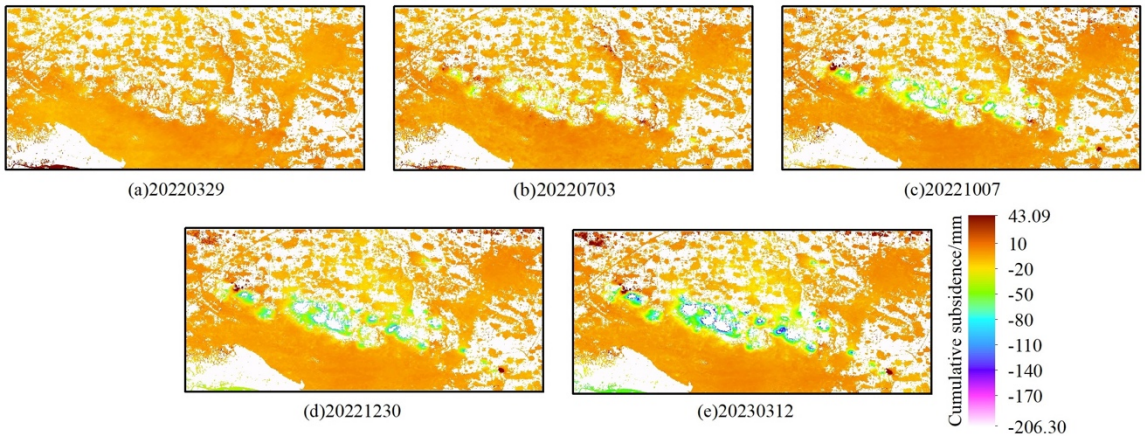

Fig. 5. Cumulative subsidence of SBAS-InSAR

Figs. 4 and 5 show that serious subsidence occurred in the center of Pingdingshan Mine from March 5, 2022, to March 12, 2023, reaching a maximum subsidence rate of -217.04 mm/a and a maximum cumulative subsidence volume of −206.3 mm. The subsidence range expanded gradually. The mining area had four subsidence regions, as shown in Fig. 4 and Table 2. Specifically, C experienced the most serious subsidence, having the largest subsidence area, many subsidence centers, and complicated surface subsidence conditions. According to the field survey control, A is located in Wangzhuang Village in eastern Baofeng County, an area affected by coal mining in the south. B is located in Bianzhuang, Xinhua District, an area affected by coal mining in the north. C is located in the border of Weidong District, Xinhua District, Baofeng County, and Jia County, covering Longshan, Xiading Village, Jijia Village, Chengzhaigou, Zhangzhai, and Zhougou Village. C has the highest number of surrounding coal production mines. D is located at the border between northern Weidong District and Xiangcheng County, covering Xiaowu Village, Majiangou Village, and Zhangzhuang Village. The area is influenced by coal exploitation in both the northern and southern regions. Many coal mines are present in Jiaodian Town south of C. However, no subsidence occurred from 2022 to 2023 because these coal mines have shut down and measures such as ecological restoration and mine filling have been adopted. The SBAS-InSAR monitoring results agreed with practical situations.

Table 2. Subsidence of four regions

Subsidence regions	Maximum subsidence rate (mm/a)	Maximum cumulative subsidence /mm
A	157	−170
B	112	−109
C	206	−217
D	189	−199

4.2 SBAS-InSAR subsidence monitoring data analysis

(1) Precision of inner coincidence verification

The standard deviation of deformation rate in the SBAS-InSAR monitoring was 1.28. The global deviation of monitoring results was low, and the stability was good.

(2) D-InSAR comparative verification

Sentinel-1A images covering Pingdingshan Mine from March 5, 2022, and March 12, 2023, were chosen for two-track D-InSAR processing. By using the image of 20220305 as the primary image and the image of 20230312 as the secondary image, we obtained the cumulative settlement diagram, as shown in Fig. 6.

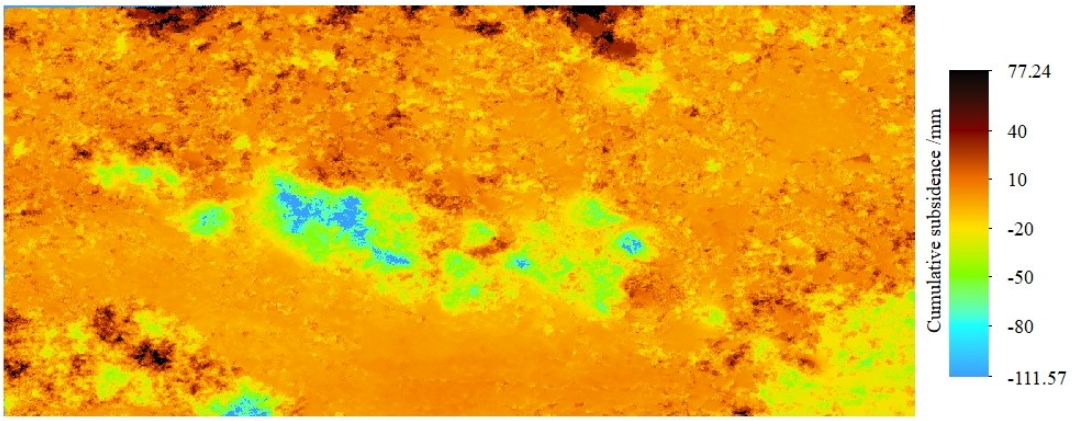

Fig. 6. Cumulative subsidence diagram of D-InSAR

A comparison with the SBAS-InSAR results in Fig. 4 indicates that D-InSAR and SBAS-InSAR showed similar positions, shapes, and size of regions with serious subsidence, and similar overall subsidence distribution. However, the maximum cumulative subsidence volume in SBAS-InSAR monitoring was far higher than that of D-InSAR. SBAS-InSAR is more sensitive to long-term subsidence monitoring in mining areas and can monitor greater subsidence gradients.

4.3 ELM subsidence prediction test of mining areas

Three characteristic points were chosen in C, which had the most serious subsidence, to verify the feasibility of ELM in surface subsidence prediction in mining areas. The subsidence time series at these three characteristic points were chosen as research objects; these three points are P1, P2, and P3. When ELM was used to build prediction model, three key parameters were applied: number of the input layer nodes, number of the hidden layer neuron, and excitation function of the ELM network. The two-dimensional interval searching algorithm was introduced to construct the optimal ELM network structure. In the experiment, P1 was chosen to determine the ELM optimal network structure.

4.3.1 Effects of node number of the input layer on network prediction performances

Twenty-one phases of data were available at P1. The 1-16 phases were chosen as the model training samples, while the 17-21 phases were chosen as test samples. On the basis of the idea of rolling prediction, the node number of the input layer increased from 3 to 12, and the output node number was fixed 1 in the optimization test. Influences of node number of the input layer on ELM network training and test samples were analyzed. Table 3 shows the results.

Table 3. RMSE of ELM network training and test samples under different number of the input layer nodes

Samples	Number of the input layer nodes									
	3	4	5	6	7	8	9	10	11	12
Modeling (RMSE/mm)	6.013	5.096	9.557	5.857	9.764	4.744	0.006	0.006	0.006	0.005
Prediction (RMSE/mm)	2.726	4.248	2.696	8.130	6.235	10.617	2.838	1.989	2.118	1.706

Table 3 shows that the RMSE of the ELM network training and test samples changes significantly with the number of the input layer nodes. The best ELM network structure is achieved when the input layer has 12 nodes.

4.3.2 Optimization of neuron number of the hidden layer and excitation function

On the basis of the above experiment, the minimum RMSE of training samples was chosen as the objective function. The two-dimensional interval searching algorithm was applied to obtain the optimal values of number of the hidden layer neuron and excitation function. The processes are shown in Figs. 7 and 8.

Table 4. ELM network modeling and prediction performance analysis

RMSE/mm	P1	P2	P3
Training samples	0.005	0.006	0.008
Test samples	1.706	2.922	2.797

Figs.7 and 8 show that the excitation function and neuron number of the hidden layer influence ELM prediction significantly. During modeling of P1, Sin and sigmoid functions are better than the hardlim function under the same neurons. When the Sin function is applied as the excitation function, the RMSE of training samples and test samples of the ELM network is the minimum. Fig. 8 shows that under the Sin function, the RMSE of prediction accuracy decreases obviously and then tends to be stable. The prediction effect is the best when there are 16 neurons in the hidden layer.

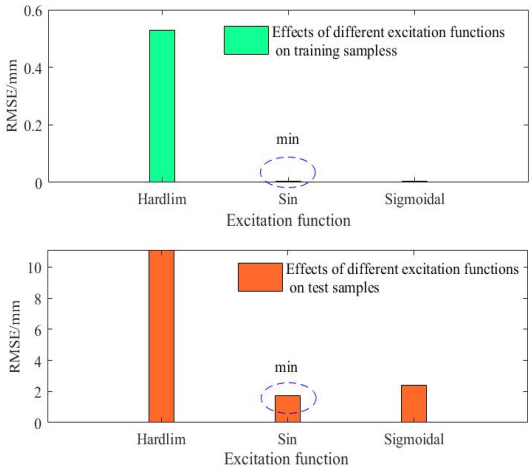

Fig. 7. Effects of excitation function on ELM prediction performances

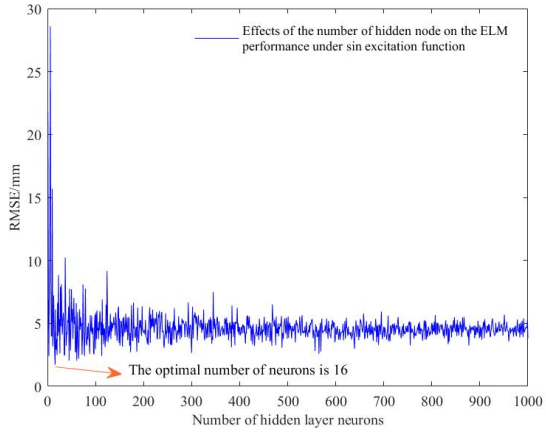

Fig. 8. Effects of number of the hidden layer neuron on ELM prediction performances

The parameter optimization of P2 and P3 can be referred to that of P1. According to the ELM model built based on the above parameters, the subsidence prediction results are shown in Table 4.

Table 4 shows that ELM prediction could achieve high accuracy for both training and test samples. For training samples, RMSE reached 10^{-3} mm, indicating that the constructed ELM model is stable and reliable. For test samples, the minimum and maximum MRE are 1.706 and 2.922 mm, respectively. Obviously, the generalization ability of ELM network is relatively strong.

4.3.3 Verification analysis of the subsidence prediction model

SVM, BP, and the proposed ELM were chosen for comparative tests to verify the advantages of ELM in subsidence prediction. The calculation process built models and implemented prediction by using the same training and test samples. Data prediction and accuracy evaluation results are shown in Tables 5-7.

Table 5. ELM subsidence prediction values and evaluation results(mm)

Sequence	Subsidence at P1	ELM prediction	Subsidence at P2	ELM prediction	Subsidence at P3	ELM prediction
17	−104.932	−106.723	−105.515	−109.738	−142.443	−146.202
18	−113.588	−113.621	−120.789	−116.215	−159.709	−157.456
19	−121.858	−119.488	−133.672	−132.192	−170.667	−166.815
20	−124.899	−124.61	−139.218	−138.956	−175.725	−175.280
21	−127.790	−130.167	−149.023	−150.317	−180.298	−182.509
RMSE		1.706		2.922		2.798
MRE		1.150%		1.991%		1.557%

Table 6. SVM subsidence prediction values and evaluation results(mm)

Sequence	Subsidence at P1	SVM prediction	Subsidence at P2	SVM prediction	Subsidence at P3	SVM prediction
17	−104.932	−105.683	−105.515	−106.274	−142.443	−146.280
18	−113.588	−110.503	−120.789	−113.351	−159.709	−156.294
19	−121.858	−113.905	−133.672	−124.519	−170.667	−166.065
20	−124.899	−118.847	−139.218	−133.167	−175.725	−176.127
21	−127.790	−123.199	−149.023	−143.064	−180.298	−185.573
RMSE		5.119		6.509		3.887
MRE		3.679%		4.414%		2.137%

Table 7. BP subsidence prediction results and evaluation results(mm)

Sequence	Subsidence at P1	BP prediction	Subsidence at P2	BP prediction	Subsidence at P3	BP prediction
17	−104.932	−115.608	−105.515	−118.532	−142.443	−154.928
18	−113.588	−127.321	−120.789	−117.216	−159.709	−164.941
19	−121.858	−134.930	−133.672	−128.699	−170.667	−169.054
20	−124.899	−125.109	−139.218	−135.213	−175.725	−167.474
21	−127.790	−123.446	−149.023	−135.728	−180.298	−174.214
RMSE		9.923		8.941		7.628
MRE		7.312%		6.163%		4.211%

Tables 5-7 and Fig. 9 indicate that during the observation period at P1, the MRE values of ELM, SVM, and BP were maintained at approximately 1%, 4%, and 7% respectively, while the corresponding RMSE values were 2 mm, 5 mm, and 9 mm. The residual fluctuation of ELM prediction was the minimum, ranging from 0.033 to 2.377 mm. The residual error of SVM prediction was relatively small, with a fluctuation range of -0.751 to 7.952 mm. The maximum residual error occurred in Phase 19. The BP residual error showed the highest fluctuation, ranging from 0.210 to 13.733 mm. Relatively large residual errors were found at Phases 17, 18, and 19.

In the observation period at P2, the MRE values of the ELM, SVM, and BP models were controlled at about 2%, 4%, and 6%, while the RMSE values were about 3, 7, and 9 mm, respectively. The residuals predicted by ELM showed little fluctuation, ranging from -4.223 to 4.574 mm. The residual error of SVM prediction exhibited the great fluctuation ranging from -13.017 to 13.295 mm. The maximum residual error occurred in Phases 17 and 21.

In the observation period at P3, the MRE values of the ELM, SVM, and BP models were controlled at about 1.5%, 2% and 4%, while the RMSE values were about 3, 4, and 8 mm, respectively. The residuals predicted by ELM showed little fluctuation, ranging from -3.759 to 3.852 mm. The residuals predicted by SVM varied widely, ranging from-5.275 to 4.602 mm, and the larger residuals appeared in stage 21. The residuals predicted by BP exhibited the greatest fluctuations, ranging from-12.485 to 8.251 mm, and the larger residuals appeared in the 17th and 20th phases.

The RMSE and MRE of ELM prediction at P1, P2, and P3 are the lowest. The MRE was controlled within 2%, and

RMSE was smaller than 3 mm. SVM had the next lowest MRE (<5%) and RMSE (<7 mm). BP prediction was relatively poor, with an MRE <8% and an RMSE <10 mm.

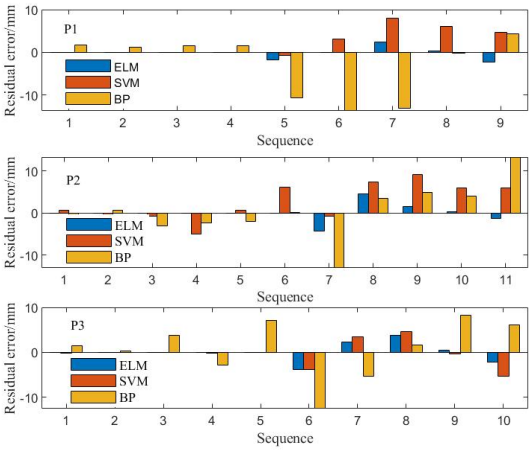

Fig. 9. Residual error comparison of different prediction models

5. Conclusions

SBAS-InSAR monitoring technology and ELM prediction are combined to realize integrated surface subsidence monitoring and prediction for high-efficiency, real-time acquisition of surface subsidence information and accurate prediction of subsidence development trend in large mining areas. An experimental study in a mining area is conducted. The following major conclusions were drawn:

(1) SBAS-InSAR has stronger adaptation than D-InSAR does. It can reflect the size and range accurately and monitor larger subsidence gradients. It can also achieve millimeter-level monitoring accuracy.

(2) During surface subsidence prediction, ELM has a simpler network than SVM and BP do. Its parameters are easy to determine, and it has a quick training speed. Moreover, ELM prediction results are stable and highly accurate. ELM avoids distortion, which exists in SVM and BP prediction.

(3) Integrating SBAS-InSAR technology and ELM prediction can provide a new, effective surface subsidence monitoring and prediction method to be used in mining areas.

In this study, the integration of SBAS-InSAR technology and ELM prediction realizes dynamic monitoring and accurate prediction of mining areas. It can provide technological references for disaster control and early warning in mining areas. Subsidence prediction of mining areas is a recursive prediction mainly based on subsidence time series, without considering influencing factors of surface subsidence, such as groundwater, and annual precipitation data. In the future, surface subsidence can be predicted with influencing factors taken into comprehensive consideration.

Acknowledgements

The authors are grateful for the support provided by the Henan Science and Technology Research Fund program (Grant No. 222102320414). We would like to show our gratitude to the website of the European Space Agency for the Sentinel-1A data in this experiment and the external DEM data of STRM.

References

[1] H. Xie, L. Wu, and D. Zheng, "Prediction on the energy consumption and coal demand of China in 2025," *J. China. Coal. Soc.*, vol. 44, no. 07, pp. 1949-1960, Aug. 2019.

[2] F. Wang, *et al*., "Monitoring of surface deformation in mining area integrating SBAS InSAR and logistic function," *Environ. Monit. Assess.*, vol. 195, no. 12, Nov. 2023, Art. no. 1493.

[3] S. Abdollahi, H. R. Pourghasemi, G. A. Ghanbarian, and R. Safaeian, "Prioritization of effective factors in the occurrence of land subsidence and its susceptibility mapping using an SVM model and their different kernel functions," *B. Eng. Geol. Environ.*, vol. 78, no. 6, pp. 4017-4034, Sep. 2019.

[4] C. Kontoes, *et al*., "Coseismic surface deformation, fault modeling, and coulomb stress changes of the March 2021 Thessaly, Greece, earthquake sequence based on InSAR and GPS Data," *Seismol. Res. Lett.*, vol. 93, no. 5, pp. 2584–2598, Jun. 2022.

[5] B. Xiao, *et al*., "Combined SBAS-InSAR and PSO-RF algorithm for evaluating the susceptibility prediction of landslide in complex mountainous area: A case study of Ludian County, China," *Sensors.*, vol. 22, no. 20, Oct. 2022, Art. no. 8041.

[6] Y. Li, *et al*., "Deformation monitoring and analysis of Kunyang phosphate mine fusion with InSAR and GPS measurements," *Adv. Space. Res.*, vol. 69, no. 7, pp. 2637-2658, Apr. 2022.

[7] G. Brencher, A. L. Handwerger, and J. S. Munroe, "InSAR-based characterization of rock glacier movement in the Uinta Mountains, Utah, USA," *Cryosphere.*, vol. 15, no. 10, pp. 4823-4844, Oct. 2021.

[8] Q. Liu, Y. Zhang, M. Deng, H. Wu, Y. Kang, and J. Wei, "Time series prediction method of large-scale surface subsidence based on deep learning," *Acta. Geod. Cattoger. Sin.*, vol. 50, no. 03, pp. 396-404, Mar. 2021.

[9] J. Aswathi, R. B. B. Kumar, T. Oommen, E. H. Bouali, and K. S. Sajinkumar, "InSAR as a tool for monitoring hydropower projects: A review," *Energy. Geosci.*, vol. 3, no. 02, pp. 160-171, Apr. 2022.

[10] F. Rafiei, S. Gharechelou, S. Golian, and B. A. Johnson, "Aquifer and land subsidence interaction assessment using Sentinel-1 data and DInSAR technique," *ISPRS. Int. J. Geo-Inf.*, vol. 11, no. 09, Sep. 2022, Art. no. 495.

[11] Z. Pérez-Falls, G. Martínez-Flores, and O. Sarychikhina, "Land subsidence detection in the Coastal Plain of Tabasco, Mexico using Differential SAR Interferometry," *Land.*, vol. 11, no. 09, Sep. 2022, Art. no. 1473.

[12] D. Ou, K .Tan, Q. Du, Y. Chen, and J. Ding, "Decision fusion of D-InSAR and pixel offset tracking for coal mining deformation monitoring," *Remote. Sens.*, vol. 10, no. 07, Jul. 2018, Art. no. 1055.

[13] M. A. Boukhemacha, *et al*., "Combined in-situ and Persistent Scatterers Interferometry Synthetic Aperture Radar (PSInSAR) monitoring of land surface deformation in urban environments-case study: tunnelling works in Bucharest (Romania)," *Int. J. Remote. Sens.*, vol. 42, no. 07, pp. 2641-2662, Jan. 2021.

[14] A. Tripathi, A. R. Reshi, M. Moniruzzaman, K. R. Rahaman, R. K. Tiwari, and K. Malik, "Interoperability of-Band Sentinel-1 SAR and GRACE satellite sensors on PSInSAR-Based urban surface subsidence mapping of Varanasi, India," *IEEE. Sens. J.*, vol. 22, no. 21, pp. 21071-21081, Nov. 2022.

[15] H. Govil, R. S. Chatterjee, P. Bhaumik, and N. Vishwakarma, "Deformation monitoring of Surakachhar underground coal mines of Korba, India using SAR interferometry," *Adv. Space. Res.*, vol. 70, no. 12, pp. 3905-3916, Dec. 2022.

[16] Y. Li, K. Yang, J. Zhang, Z. Hou, S. Wang, and X. Ding, "Research on time series InSAR monitoring method for multiple types of surface deformation in mining area," *Nat. Hazards.*, vol. 114, no. 3, pp. 2479-2508, Dec. 2022.

[17] D. A. Umarhadi, *et al*., "Use of multifrequency (C-band and L-band) SAR data to monitor peat subsidence based on time‐series SBAS InSAR technique," *Land. Degrad .Dev.*, vol. 32, no. 16, pp. 4779-4794, Oct. 2021.

[18] B. Xiao, J. Zhao, D. Zhou, W. Xi, and Z. Zhao, "Monitoring and prediction of land subsidence in Binchuan Fault Basin of Northwest Yunnan supported by SBAS-InSAR," *J. Kunming Univ. Sci. Technol (Nat. Sci)*., vol. 47, no. 03, pp. 30-39, Jun. 2022.

[19] D. Zhou and X. Zuo, "Surface subsidence monitoring and prediction in mining area based on SBAS-InSAR and PSO-BP neural network algorithm," *J. Yunnan Univ. (Nat. Sci)*., vol. 43, no. 05, pp. 895-905, Jun. 2021.

[20] B. Chen, K. Deng, and H. Fan, "Combining D-InSAR and SVR for monitoring and prediction of mining subsidence," *J. China Univ. Min. Technol.*, vol. 43, no. 05, pp. 880-886, Sep. 2014.

[21] F. Kong, T. Tian, D. Lu, B. Xu, W. Lin, and X. Du, "PSO-based machine learning methods for predicting ground surface displacement induced by shallow underground excavation method," *KSCE. J. Civ. Eng.*, vol. 27, no. 11, pp. 4948-4961, Nov. 2023.

[22] P. Berardino, G. Fornaro, R. Lanari, and E. Sansosti, "A new algorithm for surface deformation monitoring based on small baseline differential SAR interferograms,"*IEEE. Trans. Geosci. Remote.*, vol. 40, no. 11, pp. 2375-2383, Nov. 2002.

[23] G. B. Huang, Q. Y. Zhu, and C. K. Siew, "Extreme learning machine: Theory and applications," *Neurocomputing.*, vol. 70, no. 1-3, pp. 489-501, Dec. 2006.